

# Risk-Aware Aerocapture Guidance Through a Probabilistic Indicator Function

Grace E. Calkins,<sup>\*</sup> Jay W. McMahon,<sup>†</sup> and Alireza Doostan<sup>‡</sup>  
*University of Colorado Boulder, Boulder, CO 80303*

David C. Woffinden<sup>§</sup>  
*NASA Johnson Space Center, Houston, TX, 77508*

Aerocapture is sensitive to trajectory errors, particularly for low-cost missions with imprecise navigation. For such missions, considering the probability of each failure mode when computing guidance commands can increase performance. A risk-aware aerocapture guidance algorithm is proposed that uses a generative-modeling-based probabilistic indicator function to estimate escape, impact, or capture probabilities. The probability of each mode is incorporated into corrective guidance commands to increase the likelihood of successful capture. The proposed method is evaluated against state-of-the-art numeric predictor-corrector guidance algorithms in high-uncertainty scenarios where entry interface dispersions lead to nontrivial failure probabilities. When using a probabilistic indicator function in guidance, 69% to 100% of recoverable cases are saved in near-escape and near-impact scenarios. In addition, the probabilistic indicator is compared to a first-order fading memory filter for density estimation, showing improvements in apoapsis error even when a fading filter is included. The probabilistic indicator function can also accurately predict failure probability for dispersions outside its training data, showing generalizability. The proposed risk-aware aerocapture guidance algorithm improves capture performance and robustness to entry interface state dispersions, especially for missions with high navigation uncertainty.

## Nomenclature

$A_{ref}$	=	Reference area [m <sup>2</sup> ]
$a$	=	Semimajor axis [m]
$C_D$	=	Drag coefficient
$C_L$	=	Lift coefficient

---

<sup>\*</sup>Ph.D. Student, Department of Aerospace Engineering Sciences. [grace.calkins@colorado.edu](mailto:grace.calkins@colorado.edu)

<sup>†</sup>Associate Professor, Department of Aerospace Engineering Sciences.

<sup>‡</sup>Professor, Department of Aerospace Engineering Sciences.

<sup>§</sup>Aerospace Engineer, GN&C Autonomous Systems Branch

$c$	= Cluster index
$c_1, \dots, c_9$	= Polynomial atmosphere model coefficients
$F_N$	= Normal (lift) acceleration [m/s <sup>2</sup> ]
$F_T$	= Tangential (drag) acceleration [m/s <sup>2</sup> ]
$g_\phi$	= Latitudinal component of gravity [m/s <sup>2</sup> ]
$g_r$	= Radial component of gravity [m/s <sup>2</sup> ]
$h$	= Altitude above planetary surface [m]
$J_2$	= Second zonal harmonic of the planet
$\mathcal{L}$	= Variational autoencoder evidence lower bound function
$LD$	= Lift-to-drag ratio
$l$	= Number of latent variables
$m$	= Vehicle mass [kg]
$q$	= Variational posterior distribution
$R_e$	= Equatorial radius of the planet [m]
$r$	= Radius from planet center [m]
$r_a$	= Apoapsis radius [m]
$r_p$	= Periapsis radius [m]
$V$	= Planet-relative velocity [m/s]
$x$	= Gaussian mixture variational autoencoder input
$z$	= Gaussian mixture variational autoencoder latent encoding
$\beta$	= Ballistic coefficient [kg/m <sup>2</sup> ]
$\beta_{KL}$	= Variational autoencoder Kullback-Leibler divergence weighting factor
$\gamma$	= Flight path angle [rad]
$\gamma_c$	= Gaussian mixture variational autoencoder cluster membership probability
$\delta p$	= GRAM density perturbation scale
$\varepsilon$	= Specific energy [m <sup>2</sup> /s <sup>2</sup> ]
$\epsilon_C$	= Capture probability threshold
$\epsilon_F$	= Failure probability threshold
$\theta$	= Longitude [rad]
$\zeta$	= Bank angle time constant [s]
$\lambda$	= Gaussian mixture variational autoencoder decoder parameters
$\mu$	= Gravitational parameter of the planet [m <sup>3</sup> /s <sup>2</sup> ]

$\mu_c$	=	Gaussian mixture variational autoencoder cluster means
$\nu$	=	Gaussian mixture variational autoencoder encoder parameters
$\pi_c$	=	Gaussian mixture variational autoencoder cluster weights
$\rho$	=	Atmospheric density [kg/m <sup>3</sup> ]
$\rho_D$	=	Drag fading filter scaling factor
$\rho_L$	=	Lift fading filter scaling factor
$\tau$	=	Bank angle correction persistence time [s]
$\phi$	=	Latitude [rad]
$\phi_x$	=	Gaussian mixture variational autoencoder ELBO recognition network
$\phi_c$	=	Gaussian mixture variational autoencoder ELBO recognition network
$\chi$	=	Fading filter time constant
$\psi$	=	Heading angle [rad]
$\sigma$	=	Bank angle [rad]
$\sigma_c$	=	Gaussian mixture variational autoencoder cluster variances
$\sigma'$	=	Bank angle correction magnitude
$\Omega$	=	Planet rotation rate [rad/s]

## I. Introduction

**A**EROCAPTURE is an alternative to propulsive orbit insertion in which the spacecraft flies through the atmosphere of a planet to capture into orbit. Aerocapture is an attractive option for missions to ice giants as it reduces transit time and propellant requirements. The Planetary Science Decadal Survey [1] places high priority on missions to ice giants, and the proposed Uranus Orbiter Probe mission investigated aerocapture as an alternative to propulsive orbit insertion. [2] The outcome of an aerocapture trajectory is highly sensitive to atmospheric interface state dispersions, especially in flight path angle and velocity. [3] If an improper amount of energy is dissipated during atmospheric flight, the spacecraft can either impact the surface of the planet or escape from the planet's sphere of influence back into interplanetary space. This is not a concern for missions with precise navigation solutions, but less expensive missions may employ less accurate navigation solutions. For sufficiently large initial state errors, vehicle parameter dispersions, or large atmosphere uncertainty, some portions of the spacecraft's state distribution could lead to a failed trajectory, even if the predicted mean successfully captures.

The state-of-the-art fully numeric predictor-corrector aerocapture guidance algorithm (FNPAG) only considers the outcome of the nominal or mean state when computing guidance commands. [4] Brunner and Lu have shown that a numeric predictor-corrector guidance algorithm outperforms Apollo skip entry guidance (which has similar

flight regimes to aerocapture guidance) for conservative initial state dispersions, but the  $3\sigma$  velocity dispersions were  $O(10)$  m/s and the  $3\sigma$  flight path angle dispersions were roughly  $0.4^\circ$ . [5] While these values are typical for missions to date, there is significant navigation cost to obtain initial dispersions this conservative, especially for outer planet missions. [6] If the probability of the spacecraft belonging to one of the unsuccessful modes is sufficiently high, computing guidance algorithm commands based on the mean state can lead to failures. For example, if the onboard models significantly differ from the truth models, the onboard guidance models could predict a successful capture when computing guidance commands. Still, the vehicle could be escaping or impacting due to environmental dispersions. This is especially pertinent for missions with less accurate navigation systems, as the state uncertainty is higher and the terminal mode-impact, capture, or escape-is more uncertain. Incorporating a probabilistic indicator function into the guidance algorithm can improve robustness in such cases. The proposed probabilistic indicator function is lightweight and efficient, making it easy to integrate into FNPAG without increasing computational cost-thus enhancing robustness for both low- and high-uncertainty missions.

Other flight scenarios, such as skip entry guidance and launch vehicle abort guidance, include guidance triggers based on predicted flight modes. The nominal guidance mode for the Apollo capsule was a skip entry, but if the predicted skip-out velocity was less than desired, the skip-out was omitted in favor of a direct entry. [7] The Space Shuttle had several ascent abort modes in case of main engine failure, including returning to the launch site and transoceanic abort landing. [8] Mission Control selected an abort mode based on vehicle velocity, altitude, and time of engine failure. Risk-aware aerocapture guidance adopts these concepts into an autonomous, probabilistic framework to increase capture rate for aerocapture missions with high navigation uncertainty.

Previous work has focused on improving aerocapture guidance performance by improving onboard density estimation within the FNPAG framework using recurrent neural networks and the Karhunen-Loève expansion. [9–11] Other work has also been done to reformulate the entry and aerocapture guidance problems to use convex optimization techniques to allow more flexibility in the objective function and constraints. [12–14]. While these approaches can improve guidance performance and account for uncertainty, they focus on relatively small initial state dispersions and do not include failure modes (escape or impact) in the guidance decision-making process.

In the present work, a risk-aware aerocapture guidance algorithm is introduced, which uses a probabilistic indicator of trajectory mode to inform and bias guidance commands. This paper considers low lift-to-drag-ratio vehicles employing bank angle steering, using the FNPAG predictor-corrector structure. The two main components of this algorithm are the indicator function and the corrective guidance command. A Gaussian Mixture Variational Autoencoder (GMVAE) will be used as the indicator function as it is a computationally efficient clustering algorithm and, once trained, can efficiently and accurately determine modal probabilities for a given trajectory. [15] When finding the optimal bank angle to minimize target apoapsis error, the probabilistic indicator function is evaluated to determine the probability of each mode. If the modal probability of impact or escape is too high, or the modal probability of capture is too low, the

commanded bank angle is biased away from the predicted failure mode. If none of these thresholds are exceeded, the command from the numeric predictor-corrector guidance algorithm is executed.

The remainder of this paper is organized as follows. First, we outline the aerocapture problem and specifics of the scenarios investigated in this paper. Second, the FNPAG implementation specifics are discussed. Third, we detail the training and validation of the GMVAE probabilistic indicator function. Fourth, we present the risk-aware aerocapture guidance algorithm. Fifth, we present the results of the risk-aware aerocapture guidance algorithm and compare it to the FNPAG algorithm for three Monte Carlo experiments. Finally, we close with concluding remarks and future work.

## II. The Aerocapture Problem

The equations of motion over an oblate-spheroid, rotating planet for a spacecraft in the atmosphere are given by the following equations: [16]

$$\frac{dr}{dt} = V \sin \gamma \quad (1)$$

$$\frac{d\theta}{dt} = \frac{V \cos \gamma \cos \psi}{r \cos \phi} \quad (2)$$

$$\frac{d\phi}{dt} = \frac{V \cos \gamma \sin \psi}{r} \quad (3)$$

$$\frac{dV}{dt} = F_T - g_r \sin \gamma - g_\phi \cos \gamma \sin \psi + \Omega^2 r \cos \phi (\sin \gamma \cos \phi - \cos \gamma \sin \phi \sin \psi) \quad (4)$$

$$\begin{aligned} \frac{d\gamma}{dt} = \frac{1}{V} & \left( F_N \cos \sigma - g_r \cos \gamma + \frac{V^2}{r} \cos \gamma + g_\phi \sin \gamma \sin \psi \right. \\ & \left. + 2\omega V \cos \phi \cos \psi + \Omega^2 r \cos \phi (\cos \gamma \cos \phi + \sin \gamma \sin \phi \sin \psi) \right) \end{aligned} \quad (5)$$

$$\begin{aligned} \frac{d\psi}{dt} = \frac{1}{V} & \left( \frac{F_N \sin \sigma}{\cos \gamma} - \frac{V^2}{r \cos \gamma \cos \psi} \tan \phi - \frac{g_\phi \cos \psi}{\cos \gamma} \right. \\ & \left. + 2\Omega V (\tan \gamma \cos \phi \sin \psi - \sin \phi) - \frac{\Omega^2 r \sin \phi \cos \phi \cos \psi}{\cos \gamma} \right) \end{aligned} \quad (6)$$

$$\frac{d\sigma}{dt} = \frac{\sigma_{\text{command}} - \sigma}{\zeta}, \quad (7)$$

where  $r$  is the vehicle position radius relative to the center of the Earth,  $\theta$  is the longitude,  $\phi$  is the latitude,  $V$  is the planet-relative velocity,  $\gamma$  is the flight path angle (defined positive above local horizon),  $\psi$  is the heading angle,  $\Omega$  is the rotation rate of the planet,  $\sigma$  is the bank angle, and  $\zeta$  is the bank angle time constant. The radial and latitudinal components of gravity are

$$g_r = \frac{\mu}{r^2} \left( 1 + J_2 \left( \frac{R_e}{r} \right)^2 (1.5 - 4.5 \sin^2 \phi) \right), \quad (8)$$

$$g_\phi = 3 \frac{\mu}{r^2} \left( J_2 \left( \frac{R_e}{r} \right)^2 \sin \phi \cos \phi \right), \quad (9)$$

where  $\mu$  is the gravitational parameter of the planet,  $J_2$  is the second zonal harmonic of the planet, and  $R_e$  is the equatorial radius of the planet.

The aerodynamic accelerations are given by:

$$F_T = -\frac{\rho V^2}{2\beta}, \quad (10)$$

$$F_N = \frac{\rho V^2 LD}{2\beta}, \quad (11)$$

where  $\rho$  is the atmospheric density,  $\beta = \frac{m}{C_D A_{ref}}$  is the ballistic coefficient,  $LD = \frac{C_L}{C_D}$  is the lift-to-drag ratio.

In the truth model, the bank angle changes per Eq. (7). The bank angle rate is constrained to be less than 20 °/s, and if Eq. (7) calls for a higher bank angle rate, it is clipped to this constraint. However, when computing optimal guidance commands using root-finding,  $\dot{\sigma} = 0$  is used instead of Eq. (7) to solve for the optimal constant bank angle or switching time.

The nominal state initial conditions for a Uranus aerocapture are presented in Table 1. These conditions are based on the values used for the Uranus Orbiter Probe mission design. [2, 17] Two scenarios are used for this paper—near-escape and near-impact—as two Gaussian-distributed datasets are needed to represent all three modes (capture, impact, and escape) in the data. The initial flight path angle of the near-escape trajectory is in the center of the flight path angle corridor, and dispersions result in escaped cases. The initial flight path angle for the near-impact trajectory is at the bottom of the flight path angle corridor such that dispersions result in impacts. Each guidance simulation is run for 1,500 s with a 1 s time-step. The nominal vehicle has a ballistic coefficient  $\beta$  of 145 kg/m<sup>2</sup>, a lift-to-drag ratio  $LD$  of 0.25, and a nominal mass of 2847.068 kg. [2, 17]

**Table 1 Initial conditions and targets for each scenario. Note that velocity and flight path angle are given in the inertial frame.**

Description	$h_{a,target}$ [km]	$h_0$ [km]	$\theta_0$ [°]	$\phi_0$ [°]	$V_{0,I}$ [km/s]	$\gamma_{0,I}$ [°]	$\psi_0$ [°]
Near-Escape	550,000	1000	190.045	-9.764	24.936	-10.572	45
Near-Impact	100,000	1000	190.045	-9.764	24.936	-11.277	45

To generate Monte Carlo samples for GMVAE training and comparison of the guidance algorithm, the initial state and vehicle parameters are sampled from a multivariate Gaussian distribution. The standard deviations of the initial conditions are given in Table 2, and the nominal values used are described in Table 1.

Two atmosphere models are used for this study: Uranus Global Reference Atmospheric Model (UranusGRAM) samples [18] and a polynomial fit to UranusGRAM. [19] The UranusGRAM samples are drawn by varying the

**Table 2 Monte Carlo dispersions.**

Parameter	$LD$	$m$ [kg]	$h_0$ [km]	$\theta_0$ [rad]	$\phi_0$ [rad]	$V_0$ [km/s]	$\gamma_0$ [rad]
$3\sigma$	0.075	854.12	100	0.227	0.116	750	0.5

UranusGRAM random seed from  $\mathcal{U}(1, 29999)$  and using a density perturbation scale,  $\delta\rho = 2$ , for altitudes between 0 and 5,000 km. The large density perturbation scale was chosen to produce the most variability in the training data. The atmosphere is assumed to be uniform across the surface of the planet, so the latitude and longitude are held constant when drawing samples. A single UranusGRAM profile is used in the truth model, and density values are linearly interpolated from the predefined grid to the vehicle's altitude. For the onboard model, a simplified polynomial fit was found following: [19]

$$\ln \rho = \frac{c_1 + c_3 h + c_2 h^2 + c_7 h^3 + c_9 h^4}{1 + c_2 h + c_4 h^2 + c_6 h^3 + c_8 h^4}. \quad (12)$$

This higher-order polynomial fit was required rather than the commonly-used exponential because using a single exponential atmosphere fit over all the altitudes in the aerocapture flight regime yields a high mean error between the GRAM average and the exponential fit. The polynomial fit coefficients are obtained by performing a nonlinear least squares curve fit between 200 and 2,000 km altitude, and are included in Table 3.

**Table 3 Polynomial Atmosphere Model Coefficients.**

$c_1$	$c_2$	$c_3$	$c_4$	$c_5$	$c_6$	$c_7$	$c_8$	$c_9$
-1.01e+00	1.18e+07	-8.47e+07	-3.61e+01	1.81e+02	4.10e-05	-4.78e-05	1.86e-11	-7.03e-10

An escaped trajectory is defined as a trajectory with a negative final apoapsis radius,

$$r_a = a \left( 1 + \sqrt{1 - \frac{V_f^2 r_f^2 \cos^2(\gamma_f)}{\mu a}} \right), \quad (13)$$

where  $r_f$ ,  $V_f$ , and  $\gamma_f$  are the radial position, velocity, and flight path angle at atmospheric exit interface, and the semimajor axis  $a$  is

$$a = \frac{\mu}{\frac{2\mu}{r_f} - V_f^2}. \quad (14)$$

An impact trajectory is defined as either a trajectory with a periapsis radius less than 100 km, where periapsis radius is defined as:

$$r_p = a \left( 1 - \sqrt{1 - \frac{V_f^2 r_f^2 \cos^2(\gamma_f)}{\mu a}} \right), \quad (15)$$

or a trajectory with a negative terminal altitude rate (i.e. the vehicle is descending). If the altitude at time  $t_f$  is lower than the altitude at time  $t_f - \Delta t$  s, the trajectory is considered an impact trajectory.

### III. Overview of Fully Numeric Predictor-Corrector Aerocapture Guidance (FNPAG)

The FNPAG Algorithm is a state-of-the-art numeric predictor-corrector bank angle modulation aerocapture guidance algorithm. [4] In this study, FNPAG with optimal apoapsis targeting (Mode 1) with lateral logic targeting inclination is employed, as presented in Algorithm 1. To derive FNPAG, Lu proves that the optimal solution to the apoapsis targeting problem for aerocapture has a bang-bang structure, assuming that 1) the objective function is only a function of the terminal longitudinal variables ( $r_f, V_f, \gamma_f$ ) and 2) bank angle is the only control variable. [4] Because of this, an FNPAG trajectory is divided into two phases. In Phase 1, the vehicle flies at a small initial bank angle  $\sigma_0$  until the optimal switching time, after which it flies at a larger bank angle  $\sigma_f$  in Phase 2.

---

**Algorithm 1:** Fully Numeric Predictor-Corrector Aerocapture Guidance (FNPAG) Algorithm for Apoapsis Targeting. [4]

---

```

Input: Initial state  $\mathbf{x}_0$ , guidance model guidance_model, truth model truth_model
1 Initialize  $t_{\text{switch}} \leftarrow 300$  s,  $g_{\text{Lim}} \leftarrow 0.1$  Earth g,  $\sigma_0 \leftarrow 10^\circ$ ,  $\sigma_f \leftarrow 90^\circ$ ;
2 Set guidEnabled  $\leftarrow$  False, FNPAG_phase  $\leftarrow$  1;
3 while  $t_k < t_f$  do
4   Update fading filters for density estimation using Eqs. (19) and (20);
5   if  $g \geq g_{\text{Lim}}$  then
6     guidEnabled  $\leftarrow$  True;
7   else
8     guidEnabled  $\leftarrow$  False;
9   if guidEnabled then
10    Compute  $(t_{\text{switch}}, \sigma^*, \text{err})$  by solving root-finding problem using Eq. (16) with guidance model
11    guidance_model and past state  $\mathbf{x}_{k-1}$ ;
12    Compute bank angle direction based on lateral logic targeting inclination;
13    /* Get Bank Angle command based on current phase */
14    if  $t < t_{\text{switch}}$  then
15       $\sigma_{\text{command}}$   $\leftarrow$   $\sigma_0$ ;
16    else
17       $\sigma_{\text{command}}$   $\leftarrow$   $\sigma^*$ ;
18    /* Integrate truth dynamics in Eqs. 1-7 to update state */
19    Update  $\mathbf{x}_{k+1} \leftarrow \text{Integrate}(\mathbf{x}_k, \sigma_{\text{command}}, \text{truth\_model})$ ;
20    Set  $\mathbf{x}_k = \mathbf{x}_{k+1}$ ,  $k = k + 1$ ,  $t_k = t_k + \delta t$ ;
21    /* Check for phase switch */
22    if  $t > t_{\text{switch}}$  and FNPAG_phase == 1 then
23      FNPAG_phase  $\leftarrow$  2;

```

---

When the truth and guidance models are identical, the bang-bang control structure is sufficient to reach the apoapsis target. However, discrepancies between the truth and the onboard guidance model result in the vehicle failing to achieve the desired apoapsis target by maintaining a constant  $\sigma_f$  in Phase 2. This occurs because the optimal  $\sigma_f$  is found without accounting for the true parameters. To address this, in Phase 2, a bank angle that minimizes apoapsis radius error is found at each guidance cycle. This enables FNPAG to adapt to differences between the onboard guidance models and the truth models. To find the optimal switching time in Phase 1 and the optimal bank angle in Phase 2, a

root-finding problem is solved using initial bracketing and Brent's Method.[20]

Although many aerocapture studies determine the guidance command by minimizing a function of the apoapsis radius error, this analysis adopts an alternative objective function derived by equating the specific energy at atmospheric exit to the specific energy corresponding to the target apoapsis radius: [12]

$$\text{err} = \left( \frac{1}{r_f} - \frac{V_f^2}{2} \right) - \left( \frac{1}{r_{a,\text{target}}} - \frac{r_f^2 V_f^2 \cos^2 \gamma_f}{2r_{a,\text{target}}^2} \right). \quad (16)$$

In this formulation,  $J_2$  effects are assumed to be negligible. To improve numerical stability, all position quantities are nondimensionalized by the planet's equatorial radius,  $R_e$ , and velocity quantities are nondimensionalized by  $\sqrt{R_e g_0}$  following the convention of Lu et al. [21]

The truth model incorporates dispersions in vehicle parameters, atmospheric conditions, and initial conditions. While the guidance model accounts for dispersed initial conditions under the assumption of perfect navigation, it does not incorporate dispersions in vehicle and atmospheric properties. Guidance is not activated until the aerodynamic accelerations exceed a threshold of 0.1 g when the vehicle has enough control authority. The initial bank angle is set to  $10^\circ$  and the final bank angle is set to  $90^\circ$ . The guidance algorithm is run until the final time,  $t_f = 1500$  s, is reached.

Two first-order fading-memory filters using IMU data are implemented to improve onboard density estimation. The filters estimate the ratios:

$$\rho_L = \frac{L}{L^*}, \quad (17)$$

$$\rho_D = \frac{D}{D^*}, \quad (18)$$

where  $L$  and  $D$  are the true lift and drag forces measured by the IMU and  $L^*$  and  $D^*$  are the lift and drag forces computed using the onboard model. In the  $(n+1)$ -th guidance cycle, the navigation scaling factors,  $\tilde{\rho}_L^{(n+1)}$  and  $\tilde{\rho}_D^{(n+1)}$ , are updated following:

$$\tilde{\rho}_L^{(n+1)} = \tilde{\rho}_L^{(n)} + (1 - \chi)(\rho_L - \tilde{\rho}_L^{(n)}), \quad 0 < \chi < 1 \quad (19)$$

$$\tilde{\rho}_D^{(n+1)} = \tilde{\rho}_D^{(n)} + (1 - \chi)(\rho_D - \tilde{\rho}_D^{(n)}), \quad 0 < \chi < 1 \quad (20)$$

where  $\rho_L$  and  $\rho_D$  are based on the current IMU measurement,  $\tilde{\rho}_L^{(n)}$  and  $\tilde{\rho}_D^{(n)}$  are the previous estimates, and  $\chi$  is the filter time constant. The initial values for  $\tilde{\rho}_L^{(0)}$  and  $\tilde{\rho}_D^{(0)}$  are set to 1, and  $\chi = \exp(-1/6) \approx 0.84$  is used. The resultant  $\tilde{\rho}_L^{(n+1)}$  and  $\tilde{\rho}_D^{(n+1)}$  are used to scale the lift and drag accelerations in Eqs. (10) and (11) in onboard numerical integrations.

## IV. Gaussian Mixture Variational Autoencoder Training and Evaluation

A GMVAE is an unsupervised clustering and dimensionality reduction algorithm that uses a Gaussian Mixture Model (GMM) to cluster data in a lower-dimensional latent space. Thus, they are an attractive choice for the indicator function. [15, 22, 23] A variational autoencoder (VAE) is a neural network architecture based on variational Bayesian methods that encodes a large dimensional input,  $x$ , (i.e. the aerocapture trajectory) into a lower dimensional latent space,  $z$ , according to a given distribution, and then decodes the information in the latent space back to the input space. The use of deep neural networks for the encoder and decoder allows the autoencoder to leverage nonlinear relationships in the input data. A GMVAE differs from a traditional VAE as the latent space is a mixture of Gaussians instead of a single Gaussian, which allows the GMVAE to capture multi-modal distributions in the input data, shown in Fig. 1. In encoding input data to the latent space, the GMVAE can determine the probability that a given sample belongs to a certain cluster. Only the encoded latent space representation is required to determine the cluster membership probabilities, while the decoder is required for training to ensure that the latent space is an accurate representation of the input data. As shown in the figure, the decoded data can be noisier and lower variance than the input data if the GMVAE is not well-trained.

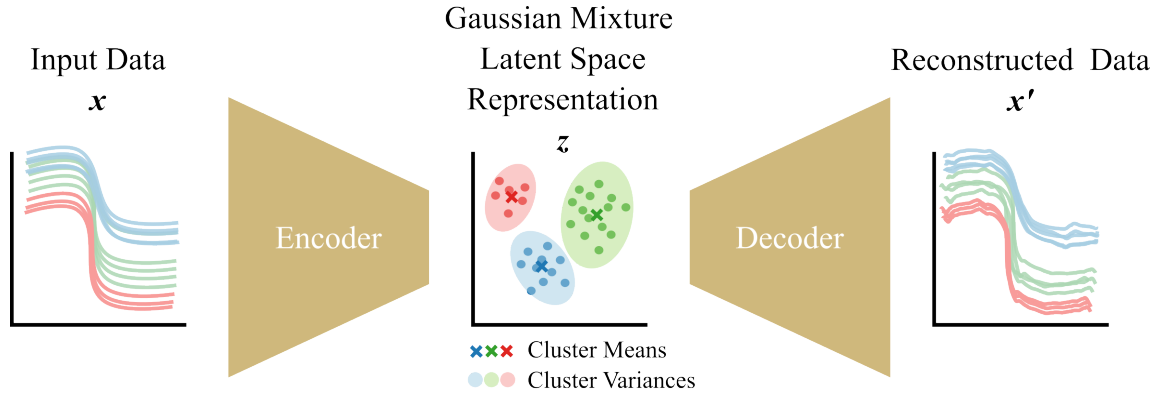


**Fig. 1 GMVAE schematic for two-dimensional latent space with three data clusters.**

The main advantage of using a GMVAE is the computational speed with which trajectory cluster membership can be determined. The GMVAE is trained to minimize the log-evidence lower boundary (ELBO), which measures how well the latent space is captured by the Gaussian mixture model and how well the decoder reconstructs the input data. This work employs a novel GMVAE framework, which estimates cluster probability through an Expectation Maximization (EM) step as part of the training. [24] In the expectation step, the cluster membership probabilities  $\gamma_c$  are found by computing the probability of a certain latent variable given a certain cluster,  $p(z|c)$ . In the maximization step, the GMM cluster means and variances  $\mu_c$  and  $\sigma_c$  are computed based on  $\gamma_c$ . A forward evaluation of the trained encoder neural network and evaluation of the expectation step is all that is needed to determine the modal probabilities for a sample  $x$ . The EM step evaluation will be discussed in detail in the following section. The EM step indirectly optimizes the ELBO:

[15]

$$\text{ELBO} = \mathbb{E}_q \left[ \frac{p_{\lambda, \nu}(x', x, c, z)}{q(x, c, z|x')} \right], \quad (21)$$

where  $x'$  is the reconstructed data,  $\lambda$  and  $\nu$  are the decoder and encoder parameters,  $p_{\lambda, \nu}$  is the joint distribution of the data and latent space, and  $q$  is the variational posterior.

The latent prior  $p(z)$  is modelled as a GMM

$$p(z) = \sum_c \pi_c \mathcal{N}(z|\mu_c, \sigma_c^2), \quad (22)$$

where  $\pi_c$  is the cluster weight or probability,  $\mu_c$  is the cluster mean, and  $\sigma_c^2$  is the cluster variance, all learned during the EM step.

Using the GMM structure of the latent space and simplifying the ELBO expression, the ELBO from Eq. (21) can be written as: [15]

$$\begin{aligned} \text{ELBO} = & \mathbb{E}_{q(x|x')} [\log p_{\nu}(x'|x)] - \mathbb{E}_{q(c|x')} \mathbb{E}_{p(z|x, c)} [\text{KL}(q_{\phi_x}(x|x') || p_{\lambda}(x|c, z))] \\ & - \text{KL}(q_{\phi_c}(c|x') || p(c)) - \mathbb{E}_{q(x|x')q(c|x')} [\text{KL}(p_{\lambda}(z|x, c) || p(z))], \end{aligned} \quad (23)$$

where  $\phi_x$  and  $\phi_c$  are recognition networks that parametrize each variational factor, and  $\text{KL}(\cdot || \cdot)$  denotes the Kullback-Leibler (KL) divergence. The terms in this expression are the reconstruction loss, conditional prior term, cluster prior term, and latent space prior term respectively.

Determining the hyperparameters that yield a GMVAE which can accurately classify trajectory modes is a nontrivial task. The GMVAE must be expressive enough to capture the variability in the input data, while also avoiding overfitting. Three main hyperparameters must be selected: the latent dimension, the neural network architecture, and the number of clusters used to fit the latent space. First, the latent dimension chosen must be large enough to describe the data modes. Second, the selected neural network architecture (i.e. number of hidden layers, hidden layer dimensions, and activation functions) must be sufficiently expressive to capture the variability in the data. Third, the number of clusters used to fit the latent space must be enough to capture the non-Gaussianity in the latent space. While theoretically there are only two clusters to describe each dataset (capture and escape or capture and impact), allowing the GMVAE to include more clusters can increase flexibility during training and improve the accuracy of the cluster probabilities (see discussion in Section II for why each dataset only includes two of the three possible modes). Each of these tuning parameters is discussed in the following sections.

### A. GMVAE Training Data and Latent Dimension Selection

Because the curse of dimensionality leads to longer neural network training times for larger dimension input data. [25] Therefore, it is beneficial to downsample the data in time and state space to reduce its dimension. For example, a 1500 s FNPAG simulation with a 1 s time step produces a trajectory in  $\mathbb{R}^{1500 \times 7}$ . To further reduce the input dimension, the training uses only the spacecraft's energy:

$$\varepsilon(t) = \frac{1}{2}V(t)^2 - \frac{\mu}{r(t)}. \quad (24)$$

As energy is positive for a hyperbolic orbit and negative for a captured orbit, this single parameter is sufficient to determine the trajectory mode: impact, capture, or escape. Terminal energy is positive for an escaped trajectory and negative for a captured or impacted one, with impacting trajectories exhibiting a large decrease in terminal energy. By using a GMVAE trained the true energy in the onboard guidance decisions, the aerocapture guidance algorithm can probabilistically account for the differences between the truth and onboard models. The energy data are downsampled to 64 evenly-spaced time steps and scaled by its initial mean to ensure all samples are approximately  $\mathcal{O}(1)$ . For trajectories which impact before the termination time, the final energy value is used to pad the remaining indices. The downsampled and scaled data for the near-escape and near-impact datasets described in Table 1 are shown in Fig. 2.

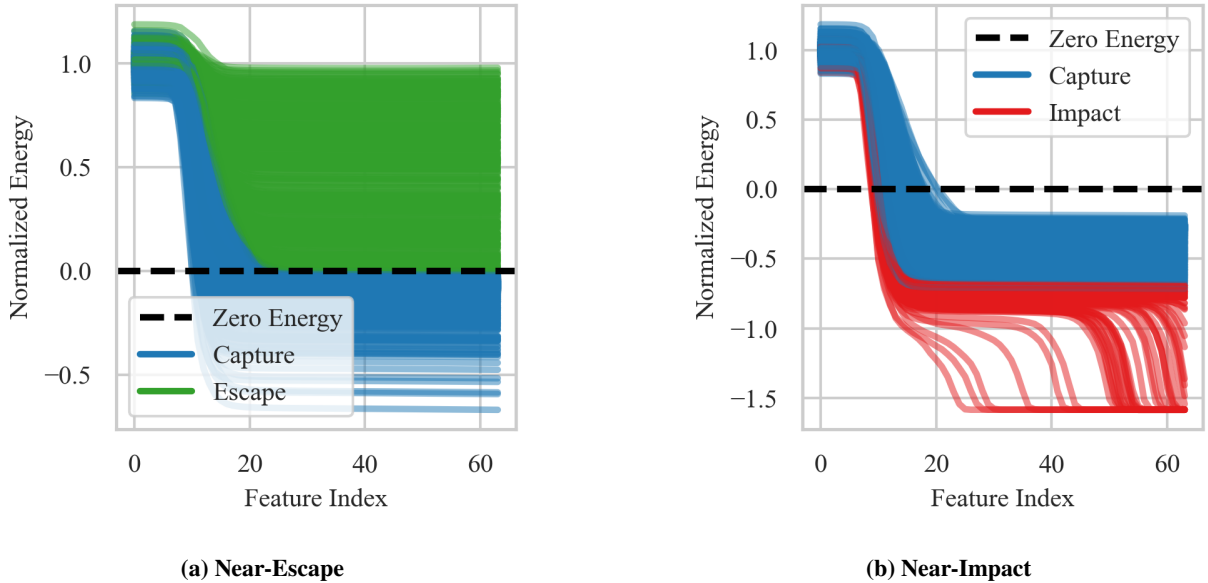


**Fig. 2** Normalized and downsampled energy training data.

To find a relatively small number of latent variables to describe the input data, singular value decomposition (SVD) is performed on the downsampled and scaled energy data. By looking at the rate of decrease of the singular value magnitudes, the dimension required to describe the input data without significant loss of information can be

determined. [26] SVD is performed on the downsampled and scaled energy data, and the singular values are shown in Fig. 3. From this data, there is a significant change in singular value magnitude after the fourth singular value for the near-impact case and after the fifth value for the near-escape case, indicating that the latent dimension of at least four or five respectively is reasonable to describe the input data.

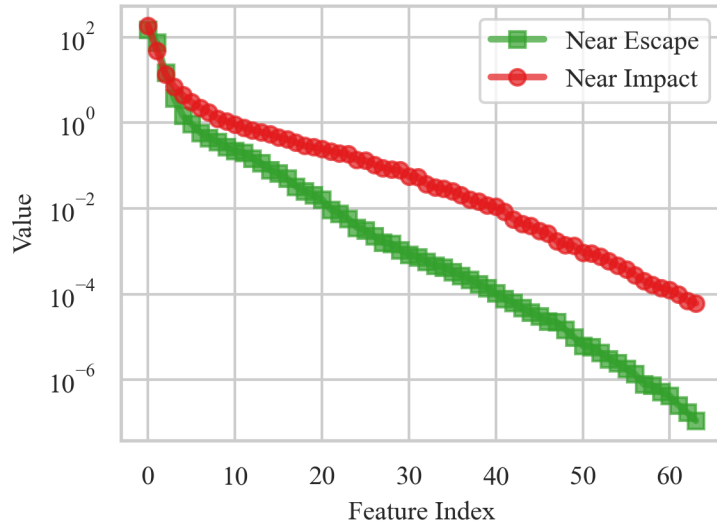


**Fig. 3 Singular values of downsampled and scaled energy data.**

## B. Neural Network Architecture Selection

To determine if the selected GMVAE encoder and decoder neural network architectures are expressive enough to describe the variability in the data, a variational autoencoder (VAE) is trained on only the capture mode of the input data. The VAE is faster to train for testing multiple neural network architectures before training the more expensive GMVAE. The VAE loss function differs from the GMVAE loss function as it does not enforce the GMM structure of the latent space. The VAE loss function is given by: [22]

$$\text{VAE Loss} = \mathcal{L}(x, x') + \beta_{\text{KL}} \sum_j \text{KL}(q_j(z|x) || p(z)), \quad (25)$$

where  $\mathcal{L}(x, x')$  is the ELBO to represent reconstruction loss and  $\beta_{\text{KL}}$  is a hyperparameter that weights the Kullback-Leibler divergence term. To determine if the encoder and decoder are a sufficient function approximation for the input data, the variance of the generated samples from the decoder is compared with the variance of the input data.

Variance loss is a common issue with VAEs, where the variance of the generated data is lower than the variance of the input data. [27] This issue can be remedied by increasing the number of hidden layers and their dimensions and varying activation functions until the generated data variance is close to the input data variance. Two to three hidden

layers of dimensions from 16 to 48 were tested with between four and seven latent variables. The best performing near-impact VAE was trained with  $\beta_{KL} = 0.0013$  and a latent dimension of six; the best performing near-escape VAE was trained with  $\beta_{KL} = 0.0015$  and a latent dimension of 6. Both models were trained for 2,000 epochs with a minibatch size of 128. The variance of the generated data is compared to the variance of the input data in Fig. 4. The variance of the generated data closely matches the variance of the input data, indicating that the VAE architecture is expressive enough to capture the variability in the input data.

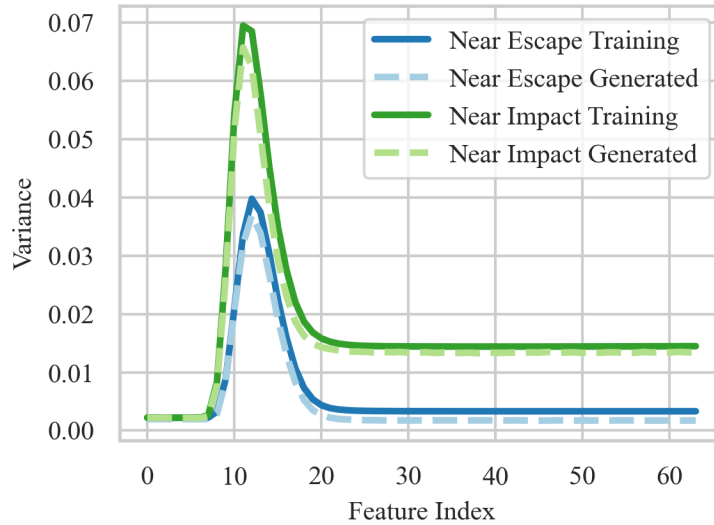


**Fig. 4 Variance difference between VAE-generated and input data.**

The encoder and decoder architectures selected for the GMVAE are shown in Fig. 5, which consist of two hidden layers with 32 and 16 neurons respectively. A Gaussian Error Linear Unit (GELU) function is used between hidden layers.

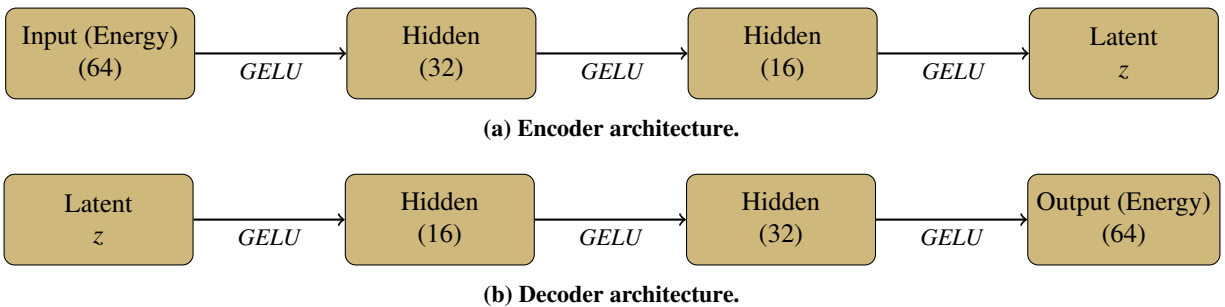


**Fig. 5 GMVAE encoder and decoder architectures with two hidden layers.**

### C. GMVAE Hyperparameter Selection

While SVD analysis found the minimum number of latent variables required to describe the input data (via linear dimensionality reduction), and a priori there are two modes in each dataset, varying these parameters can allow the GMVAE more flexibility to fit to the data. Because the encoder and decoder architecture was evaluated using a VAE in the prior section, the number of hidden layers, their dimensions, and activation functions can be held constant in the following evaluations.

To determine the best GMVAE for each dataset, the latent dimensions and number of clusters were varied. The latent dimensions were varied between four and six for the near-impact case and between five and seven for the near-escape case, and the number of clusters were varied between 2 and 6 for both trials. To compare each parameter combinations, neural network training was set to be deterministic. Each of the 15 GMVAEs was trained for 10,000 epochs with a batch size of 128 and a learning rate of 0.001. The training data were split into 1024 training samples, 128 validation samples, and 128 test samples. The Adam optimizer was used to optimize the GMVAE loss function, defined as the ELBO in Eq. (21).

To determine which mixands belong to which true cluster when the GMVAE is trained with more than two clusters, the Mahalanobis distance from each encoded sample to each cluster is computed for all samples. The mixand is assigned to the cluster with the minimum mean Mahalanobis distance across all samples.

To be effective as a probabilistic indicator function in  $\pi$ PAG, the GMVAE must accurately label the data. Misclassification percentage for each mode is defined as  $100 \times N_{\text{misassigned}}/N_{\text{cluster}}$ , where  $N_{\text{misassigned}}$  is the number of samples in a given cluster that are misassigned to the wrong mode and  $N_{\text{cluster}}$  is the true total number of samples in that cluster. The average misclassification percentage across all modes is shown for the near-impact dataset in Table 4 and for the near-escape dataset in Table 5, where  $c$  is the number of clusters and  $l$  is the latent dimension.

**Table 4 GMVAE misclassification percent error for near-impact dataset.**

	$c = 2$	$c = 3$	$c = 4$	$c = 5$	$c = 6$
$l = 4$	50.0000	32.2917	32.2917	32.2917	32.3179
$l = 5$	8.1145	25.4202	48.9583	1.9870	33.3333
$l = 6$	50.0000	20.0018	3.3438	32.2917	31.7708

**Table 5 GMVAE misclassification percent error for near-escape dataset.**

	$c = 2$	$c = 3$	$c = 4$	$c = 5$	$c = 6$
$l = 5$	3.8719	1.2473	1.0745	2.9801	3.1457
$l = 6$	5.4181	20.8609	4.9909	1.4717	2.0162
$l = 7$	4.3380	0.9162	1.0928	1.0928	1.0045

For the near-impact dataset, the GMVAE with a latent dimension of five and five clusters has the lowest percent error

of 1.9870%. For the near-escape dataset, the GMVAE with a latent dimension of seven and three clusters has the lowest percent error of 0.9162%. In both cases, the percent error is below 2%, indicating that the GMVAE can accurately predict cluster membership probabilities. These results suggest that the selected GMVAE models are sufficiently accurate to serve as probabilistic indicator functions within the aerocapture guidance algorithm. To ensure convergence, each well-performing GMVAE was further trained for an additional 20,000 epochs.

Principal component analysis (PCA) of first two modes of the latent space for both models shows that the GMVAE clusters agree with the truth mappings, as shown in Fig. 6. The data points are colored by their true cluster membership. While only the first two modes of the five- or seven-dimensional latent spaces are presented here, note that the absent modes also show good agreement between the data points and cluster means and variances. The latent spaces are clearly non-Gaussian, and allowing the GMVAE to train with more than the prescribed two clusters creates a more flexible model that can better fit the data. These mappings also reveal the cause of the misclassifications seen above. There are a some escape cases mapped near the bottom of the capture cluster for the near-escape dataset, and the large impact cluster in the near-impact model overlaps with the capture cases. While further hyperparameter tuning could improve the misclassification rates, the current GMVAE models are sufficient for the probabilistic indicator function, as guidance parameters can be adjusted to account for the misclassifications.

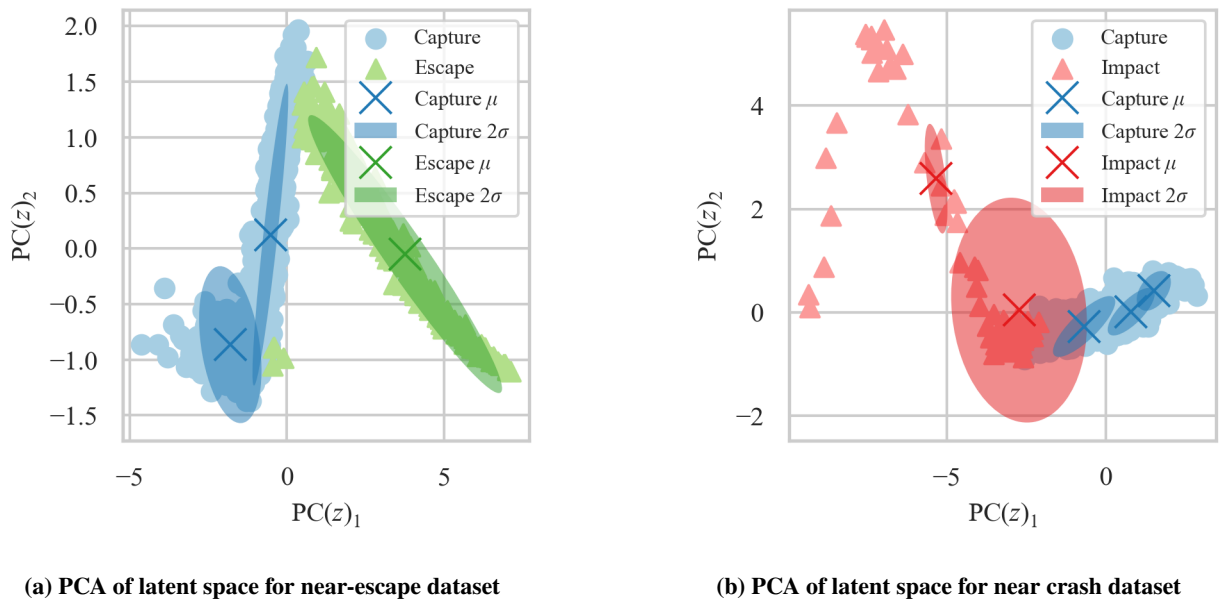


**Fig. 6** Principal component analysis of the GMVAE latent space for both datasets.

## V. Probabilistic Indicator Aerocapture Guidance Algorithm

While FNPAG is a robust guidance algorithm, all guidance decisions are made based on the onboard mean state. Discrepancies between the onboard guidance and truth models can lead to suboptimal guidance decisions, especially

when the vehicle is near the boundary between successful capture and escape. The use of a probabilistic indicator allows the guidance algorithm to account for the differences in these models and execute guidance decisions to increase the likelihood of successful capture. The GMVAE is particularly suitable for this task because it can efficiently cluster trajectory data and provide accurate modal probabilities.

### A. Probabilistic Indicator Function Evaluation

This GMVAE training algorithm uses an EM step during training to estimate cluster probabilities, and the expectation portion of that algorithm will be leveraged within the guidance algorithm to determine the cluster membership probabilities for a given trajectory. [24] To find the cluster membership probabilities for sample  $x$ , posterior probability  $p(c|z)$  is evaluated via Bayes rule:

$$p(c|z) = \frac{p(z|c)p(c)}{p(z)}, \quad (26)$$

where  $z$  is the sample of latent variables corresponding to  $x$ , and the prior probability of cluster  $c$  is  $p(c) = \pi_c$ . The likelihood of the latent sample  $z$  under cluster  $c$  is given by  $p(z|c) = \mathcal{N}(z|\mu_c, \sigma_c^2)$ . The marginal probability of  $z$  is  $p(z) = \sum_k \pi_k \mathcal{N}(z|\mu_k, \sigma_k^2)$ .

The membership probabilities for a sample  $x$  are computed in the expectation step as follows:

- 1) Encode the sample  $x$  to get the mean  $\mu$  and log variance  $\log \sigma^2$  of the latent distribution  $q(z|x)$ , the approximate posterior over  $z$ .
- 2) Compute the Log Probabilities of Each Cluster:

$$\log p(z, c) = \log \pi_c + \log \mathcal{N}(z|\mu_c, \sigma_c^2). \quad (27)$$

- 3) Apply Bayes rule to obtain the posterior  $p(c|z)$ :

$$\gamma_c = p(c|z) = \frac{p(z, c)}{\sum_k p(z, k)}. \quad (28)$$

As the nominal trajectory is already integrated forward in time during the prediction step of the FNPAG algorithm, the only additional operations to use the GMVAE indicator function are encoding the predicted trajectory through the neural network and evaluating the cluster membership probabilities for the predicted trajectory with the above steps. These operations are computationally efficient and can be done in real-time. The probabilistic indicator function is incorporated into guidance by evaluating Algorithm 2 after line 10 in Algorithm 1. When Algorithm 1 and 2 are used in conjunction, it is referred to as Probabilistic Indicator Predictor-Corrector Aerocapture Guidance ( $\pi$ PAG).

After encoding the as-flown and predicted trajectory with the GMVAE, the cluster membership probabilities  $\gamma_c$  are computed using expectation maximization. If the capture probability is below  $\epsilon_C$ , or the escape or impact probability is

---

**Algorithm 2:** Indicator Function Evaluation in  $\pi$ PAG

---

**Input:** Predicted trajectory  $\mathbf{x}_{t_k:t_f}$ , trajectory history  $\mathbf{x}_{t_0:t_k}$ , GMVAE encoder `encoder`, learned cluster probabilities  $\pi_c$ , learned cluster means  $\mu_c$ , learned cluster variances  $\sigma_c$ , capture and failure probability thresholds  $\epsilon_C$  and  $\epsilon_F$ , computed guidance command  $\sigma^*$ , guidance phase `phase`, bank correction magnitude  $\sigma'$ , persistence time  $\tau$ , last bank correction time  $t_c$

**Output:** Capture and escape probabilities  $\mathbb{P}(\text{capture})$  and  $\mathbb{P}(\text{failure})$ , corrected guidance command  $\sigma^{*'}$

- 1 Combine trajectory history and prediction to get  $\mathbf{x}_{t_0:t_f}$ , downsample to 64 predetermined time steps, compute trajectory energy at these points, and normalize to obtain input  $x$  ;
- 2 Encode  $x$  to get  $z$  using `encoder`;
- 3 Compute  $\log p(z, c)$  for each cluster  $c$  using  $\pi_c$ ,  $\mu_c$ , and  $\sigma_c$  with Eq. (27), then compute  $\gamma_c = p(c|z)$  for each cluster  $c$  with Eq. (28);
- 4 `bank_corrected = False`;
- 5 **if**  $\mathbb{P}(\text{capture}) < \epsilon_C \vee \mathbb{P}(\text{failure}) > \epsilon_F$  **then**
- 6     **if** `phase == 1` **then**
- 7         Force switch to phase 2;
- 8     **else**
- 9         Correct bank angle command  $\sigma^{*'}$  by  $\sigma'$  in the direction of  $\sigma^*$ ;
- 10         `bank_corrected = True`;
- 11          $t_c = t_k$ ;
- 12 **if** `bank_corrected = False` and  $t_k - t_c < \tau$  **then**
- 13     Correct bank angle command  $\sigma^{*'}$  by  $\sigma'$  in the direction of  $\sigma^*$ ;

---

above  $\epsilon_F$ , a corrective guidance action is applied. If guidance is in phase 1, the algorithm will force a switch to phase 2 to solve for the optimal bank angle. This indicates that the vehicle should have already been flying lift-down (in the near-escape case) or lift-up (in the near-impact case). If the guidance is in phase 2, the bank angle command is corrected by correction factor  $\sigma'$  in the direction of the predicted bank angle command  $\sigma^*$ . If the vehicle has a high escape probability, the bank angle is corrected to be more lift-down, and if the vehicle has a high impact probability, the bank angle is corrected to be more lift-up. The corrected bank angles are clipped at  $180^\circ$  when the bank angle is corrected to be more lift-down and at  $0^\circ$  when the bank angle is corrected to be more lift-up.

This algorithm also uses a persistence time  $\tau$  to prevent a bang-off-bang structure in the bank angle command as the predicted probability can oscillate between the two modes. If it is within  $\tau$  seconds of the last bank angle correction, the bank angle command is corrected by  $\sigma'$  in the direction of the predicted bank angle command  $\sigma^*$ . This prevents the algorithm from rapidly oscillating between corrected and uncorrected bank angles, as the guidance correction alters cluster membership probability. In addition, as the GMVAE is probabilistic, the persistence time allows the algorithm to account for the uncertainty in cluster membership probabilities and ensure more trajectories are saved.

While using a fixed bank correction magnitude and persistence time is an effective way to implement the probabilistic indicator function (as shown in the next sections), this is not the only or best way to implement a probabilistic indicator function for aerocapture guidance. Other schemes—such as a variable bank angle correction magnitude or persistence time based on the cluster membership probabilities—could be implemented to improve performance. Future work will focus on these options.

## B. $\pi$ PAG Performance in a Near-Escape Scenario

To demonstrate how  $\pi$ PAG algorithm can save failed FNPAG trajectories, the performance of FNPAG and  $\pi$ PAG is compared for a single near-escape scenario. The perturbations for this specific scenario are shown in Table 6, and a GRAM profile generated using the parameters described in Section II is used. When using FNPAG, these initial conditions result in an escape trajectory; however,  $\pi$ PAG is able to correct the trajectory and achieve a successful capture.

**Table 6 Initial conditions and parameter dispersions for off-nomial scenario.**

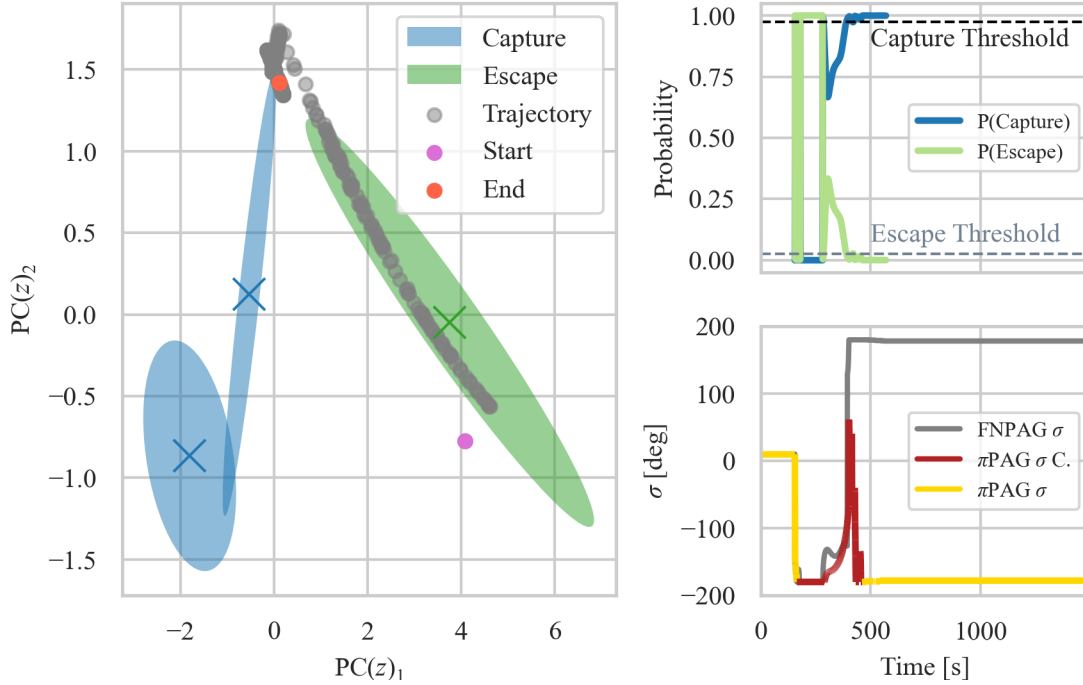
$h_0$ [km]	$V_{0,I}$ [km/s]	$\gamma_{0,I}$ [rad]	$\psi_{0,I}$ [rad]	$\theta_0$ [rad]	$\phi_0$ [rad]	$m$ [kg]	$C_L$
1011.98	27241.41	-9.70	44.99	190.05	-9.69	2.88e+03	0.24

Fig. 7 shows the trajectory evolution in the latent space, cluster membership probabilities, and bank angle commands for both FNPAG and  $\pi$ PAG. The  $\pi$ PAG parameters used for this scenario are  $\epsilon_C = 0.975$ ,  $\epsilon_F = 0.025$ ,  $\sigma' = 40^\circ$ , and  $\tau = 40$  s. The  $\pi$ PAG bank angle commands are colored based on whether a correction is applied: red indicates corrected commands, while yellow indicates uncorrected commands, corresponding to high capture probability. Initially, the trajectory has a high escape probability and is near the escape cluster in latent space. As the guidance applies corrective bank angles (shown in red), the escape probability decreases while the capture probability increases. Compared to FNPAG,  $\pi$ PAG commands a bank angle magnitude closer to  $180^\circ$ , flying more lift-down and resulting in a successful capture. This outcome is reflected in the terminal position in latent space, which lies near one of the capture clusters.

Because the indicator function predicts that this scenario is likely to escape, the  $\pi$ PAG algorithm is able to correct the trajectory and achieve a successful capture, even as the onboard guidance model does not account for true environment dispersions. While the apoapsis error and required propellant for the resultant FNPAG trajectory are undefined because the trajectory is hyperbolic, the apoapsis error and required propellant for the  $\pi$ PAG trajectory are approximately 266,000 km and 221.93 m/s respectively. While this error is large, the required  $\Delta v$  is within the expected range for proposed ice giant aerocapture missions (and still significantly lower than that required for a propulsive orbit insertion maneuver). [28]

This case highlights several noteworthy features of the  $\pi$ PAG implementation. First, it demonstrates the value of incorporating a persistence time into the algorithm. The persistence time allows the algorithm to smooth the bank angle command and prevent rapid oscillations between corrected and uncorrected bank angles. Second, the bank angle command is corrected during a bank reversal around  $t = 475$  s, shifting the target from  $180^\circ$  to  $-180^\circ$ . This reveals a shortcoming of the current  $\pi$ PAG implementation, as the bank angle correction is applied after computing the optimal bank angle but before evaluating lateral logic. Incorporating lateral logic into future versions of  $\pi$ PAG could address this issue and further improve performance.

This scenario illustrates the benefits of the probabilistic nature of the GMVAE indicator function. Even though the GMVAE is trained only on truth energy data, it is able to classify the trajectory mode using composite data from



**Fig. 7** Principal component analysis of the latent space trajectory, cluster membership probability, and bank angle command between  $\pi$ PAG and FNPAG for a near-escape case.

the as-flown trajectory and the predicted trajectory. Even though the onboard model differs from the truth model, the GMVAE can still provide accurate cluster membership probabilities.

## VI. Comparison to the State-of-the-Art Aerocapture Guidance

The proposed  $\pi$ PAG guidance algorithm is evaluated against the state-of-the-art FNPAG algorithm across a range of representative aerocapture scenarios. Three applications of  $\pi$ PAG are presented. First, the performance of  $\pi$ PAG is compared to FNPAG for both the near-impact and near-escape scenarios. This analysis demonstrates that corrective guidance actions can be taken to save impact and escape cases. Second, the performance of  $\pi$ PAG and FNPAG is compared with and without a fading filter for density estimation, highlighting the added benefit of combining a probabilistic indicator function with a fading memory filter. Finally,  $\pi$ PAG is shown to be generalizable to data outside its training data, demonstrated by training the GMVAE on lower uncertainty data and evaluating its performance in guidance with higher uncertainty dispersions. This shows that  $\pi$ PAG can be effective even when the data used for GMVAE training are not representative of the true environment.

## A. $\pi$ PAG Impact and Escape Recovery

Outer planet aerocapture missions generally target high apoapsis radius orbits to reduce the risk of impact. [2] Large dispersions in initial state and vehicle parameters will lead to some escaped trajectories when targeting the middle of the flight path angle corridor and a high apoapsis radius orbit. While it is unlikely to target a low apoapsis radius orbit from a mission design perspective to avoid impact, a scenario with a steep entry flight path angle and low apoapsis radius orbit was chosen to demonstrate the ability of  $\pi$ PAG to recover impact cases. While the near-impact scenario is not realistic for outer planet aerocapture missions, it is a useful test case to demonstrate the ability of  $\pi$ PAG to recover impact cases, and other planet's atmospheres with lower densities could lead to impact cases. The nominal initial conditions for these two scenarios are shown in Table 1.

While  $\pi$ PAG can correct for some failures, it cannot recover all failed cases. Because of the large dispersions used in this work, some trajectories will escape or impact regardless of the guidance correction applied. Therefore, the remaining analysis will focus on the percentage of recoverable trajectories saved by  $\pi$ PAG. To determine which initial conditions, atmosphere profiles, and vehicle parameter dispersions are recoverable, the vehicle is flown with either full lift-up or full lift-down from guidance start time, depending on whether the trajectory escaped or impacted. FNPAG trajectories that impacted are flown full lift-up, and FNPAG trajectories that escaped are flown full lift-down. If the mode of the trajectory changes with this guidance scheme, the trajectory is considered recoverable. If the trajectory does not change modes, it is considered unrecoverable. The recoverable save percentage for  $\pi$ PAG is computed as the number of recoverable cases that captured when using  $\pi$ PAG divided by the total number of recoverable trajectories.

This implementation of a probabilistic indicator function has three tuning parameters: the capture and failure probability thresholds  $\epsilon_C$  and  $\epsilon_F$ , the bank correction magnitude  $\sigma'$ , and the persistence time  $\tau$ . Smaller bank correction magnitudes and shorter persistence times will lead to more conservative corrections. If these parameters are too small,  $\pi$ PAG will not be able to recover all failed cases. If these parameters are too large,  $\pi$ PAG can overcorrect, causing a previously escaped case to impact. To determine the optimal parameters for  $\pi$ PAG for this problem,  $\epsilon_C$  was varied as from 0.975 to 0.99 in 0.005 increments,  $\sigma'$  was varied from  $10^\circ$  to  $40^\circ$  in  $10^\circ$  increments, and  $\tau$  was varied from 0 to 40 s in 10 s increments.

Fig. 8 shows the number of captured trajectories for near-escape cases with varying  $\sigma'$  and  $\tau$ . All simulations were run using a first-order fading filter. The number of captured trajectories was invariant to the capture threshold  $\epsilon_C$ , so it is not included on this plot. As expected, increasing the bank correction magnitude  $\sigma'$  and persistence time  $\tau$  leads to more captured trajectories. There are 42 recoverable trajectories out of a 2,000 sample Monte Carlo, and  $\pi$ PAG recovers up to 29 with a  $40^\circ$  bank correction and 40 s persistence. Looking at the 13 cases which  $\pi$ PAG did not recover: in 5 cases the GMVAE was not activated early enough in the trajectory to correct the bank angle; in 5 cases the GMVAE was not activated at all; and in 3 cases the GMVAE was activated, but the bank correction was not sufficient to recover the trajectory. The first two scenarios could be solved by developing a more accurate GMVAE model, while the third

scenario could be solved by increasing the persistence time. While further tuning of the parameters could improve the recovery rate, the current implementation of  $\pi$ PAG is sufficient to recover many escaped cases. For the following analyses,  $\pi$ PAG was implemented using  $\epsilon_C = 0.975$ ,  $\epsilon_F = 0.025$ ,  $\sigma' = 40^\circ$ , and  $\tau = 40$  s for the near-escape scenario.

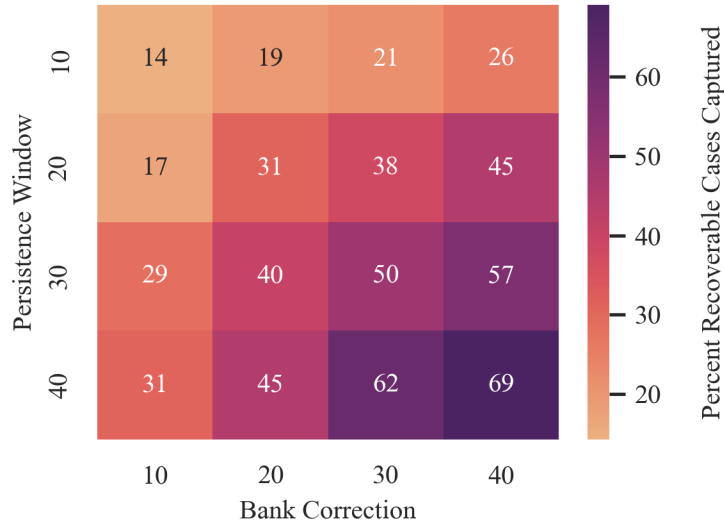


**Fig. 8** Percent of recoverable cases captured for the near-escape dataset with varying  $\sigma'$  and  $\tau$ . Capture percentage was not impacted by the capture threshold  $\epsilon_C$ .

For the near-impact scenario, all  $\pi$ PAG parameter combinations were able to recover all 18 of the recoverable trajectories. This indicates  $\pi$ PAG is more robust to the near-impact scenario, likely because the near-impact GMVAE model is more conservative. The near-impact GMVAE model assigns some captures to the impact cluster because of the overlap in the latent space (see Fig. 6b). While this leads to a higher misclassification rate, it also indicates that this GMVAE is better at catching trajectories that are near the boundary between capture and impact and correcting before they impact. For the near-impact scenario, the parameters  $\epsilon_C = 0.975$ ,  $\epsilon_F = 0.025$ ,  $\sigma' = 10^\circ$ , and  $\tau = 10$  s will be used for the following analyses.

### 1. $\pi$ PAG Escape Recovery

Monte Carlo simulations with 2,000 samples and the same initial dispersions (sampled from Table 2) were run using both FNPAG and  $\pi$ PAG for the near-escape initial conditions. The results of these simulations are shown in Table 7.  $\pi$ PAG results in a higher capture rate and lower mean apoapsis radius error and standard deviation for captured trajectories. The apoapsis radius error is defined as the difference between the apoapsis radius of the captured trajectory and the target apoapsis radius. While 13.60% of trajectories still escape with  $\pi$ PAG, the majority of these trajectories are unrecoverable. Of the 69 recoverable trajectories that escaped using FNPAG,  $\pi$ PAG captures 42 of them.

Because  $\pi$ PAG is applying a correction to the “optimal” command computed using FNPAG, it is possible that the

**Table 7 Near-escape  $\pi$ PAG and FNPAG performance comparison.**

	Capture %	Escape %	Recoverable Save %	Mean Capture $r_a$ Err. [km]	Capture $\sigma_{r_a}$ [km]
FNPAG	84.90	15.10	0.00	1.76e+05	1.59e+06
$\pi$ PAG	86.40	13.60	69.05	1.16e+05	1.02e+06

apoapsis error would decline when using  $\pi$ PAG. In addition, flying lift-down for too long could result in an impact for certain initial conditions. However, this is not the case for this combination of guidance parameters in  $\pi$ PAG, as no trajectories impact, and the captured apoapsis radius error is lower than FNPAG. This can be seen in Fig. 9, which shows the apoapsis radius error histogram for captured trajectories.  $\pi$ PAG results in fewer overshoots and more undershoots than FNPAG, which is expected as  $\pi$ PAG is correcting the bank angle command to be more lift-down.

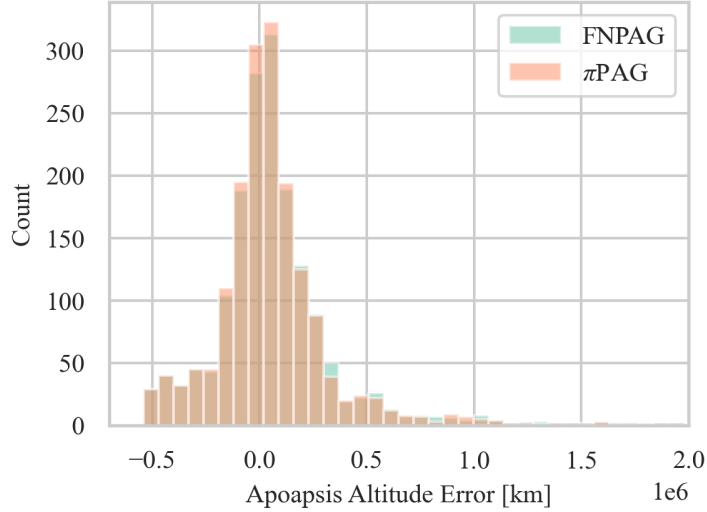


**Fig. 9 Captured apoapsis error histogram comparing  $\pi$ PAG and FNPAG for near-escape cases.**

## 2. $\pi$ PAG Impact Recovery

Monte Carlo simulations with 2,000 samples were conducted using both FNPAG and  $\pi$ PAG for the near-impact initial conditions, with initial state dispersions drawn from Table 2. The results are summarized in Table 8. As discussed earlier,  $\pi$ PAG successfully recovers all 18 of the recoverable trajectories. However, unlike in the near-escape scenario—where  $\pi$ PAG improved both apoapsis error and  $\Delta v$  accuracy—it does not yield improvements in these metrics for the near-impact case. This outcome is attributed to two primary factors. First, the recovered  $\pi$ PAG trajectories begin with lower energy and thus result in lower apoapsis radii. The mean apoapsis radius error reported in Table 8 reflects this, as it includes a larger number of captured cases with lower radii compared to FNPAG. Second, the GMVAE model selected for the near-impact scenario is more conservative than the one used in the near-escape case, assigning some captured trajectories to the impact cluster. As a result, certain trajectories that do not require correction are

unnecessarily adjusted, which can increase apoapsis error and demand more  $\Delta v$  for post-capture corrections.

**Table 8 Near-impact  $\pi$ PAG and FNPAG performance comparison.**

	Capture %	Impact %	Recoverable Save %	Mean Capture $r_a$ Err. [km]	Capture $\sigma_{r_a}$ [km]
FNPAG	95.20	4.80	0.00	-2.83e+04	3.31e+04
$\pi$ PAG	96.10	3.90	100.00	-2.84e+04	3.32e+04

### B. $\pi$ PAG Comparison to FNPAG with First-Order Fading Filter

In the previous section,  $\pi$ PAG was shown to improve performance over FNPAG in terms of both apoapsis error and number of captured trajectories for a near-escape scenario. These prior analyses were performed using first-order fading memory filters, which have been shown to improve aerocapture guidance performance in the presence of uncertainty. [4, 29] These filters improve performance by accounting for the difference between the onboard atmosphere model and the true atmosphere. Because density is a major source of uncertainty in aerocapture, improving density knowledge with a fading filter can improve overall aerocapture performance.

This probabilistic indicator function is not directly designed to improve apoapsis targeting accuracy by improving density estimation; rather it is designed to improve the aerocapture success rate by correcting trajectories that would otherwise escape or impact. However, the analysis in Section VI.A shows that  $\pi$ PAG can improve apoapsis radius error for near-escape cases when using a fading filter.

A 2,000-sample Monte Carlo simulation was run for the near-escape scenario using FNPAG with and without a first-order fading filter and  $\pi$ PAG with and without a first-order fading filter. Results are shown in Table 9. The fading filter improves capture rate for FNPAG, and also recovers the 0.6% impacted cases. FNPAG with the fading filter also improves the mean capture apoapsis radius error by two orders of magnitude over FNPAG without the fading filter.

**Table 9 Near-escape  $\pi$ PAG and FNPAG performance comparison with and without a first-order fading filter.**

	Capture %	Escape %	Impact %	Recoverable Save %	Mean Capture $r_a$ Err. [km]	Capture $\sigma_{r_a}$ [km]
FNPAG	81.15	18.25	0.60	0.00	1.12e+05	5.37e+06
FNPAG, FF	84.90	15.10	0.00	0.00	1.76e+05	1.59e+06
$\pi$ PAG	83.90	16.10	0.00	59.52	4.49e+04	2.31e+06
$\pi$ PAG, FF	86.40	13.60	0.00	85.19	1.16e+05	1.02e+06

While  $\pi$ PAG without a fading filter recovers more cases than FNPAG without a fading filter, it does not improve over FNPAG with a fading filter. However,  $\pi$ PAG with a fading filter improves capture rate over FNPAG with a fading filter. While both FNPAG and  $\pi$ PAG without the fading filter have lower mean capture apoapsis radius error than their counterparts with the fading filter, they have much larger standard deviations. This is shown in Fig. 10, where the datasets without the fading filter exhibit greater variability and more apoapsis altitude undershoot.

Because  $\pi$ PAG without a fading filter does not improve over FNPAG with a fading filter in apoapsis error or capture rate, a probabilistic indicator function is not a pure replacement for a first-order fading filter. While the fading filter improves apoapsis radius error variability,  $\pi$ PAG improves the capture rate and recovers failure cases. Thus, these two tools can be used in conjunction to improve aerocapture performance for high-uncertainty scenarios.

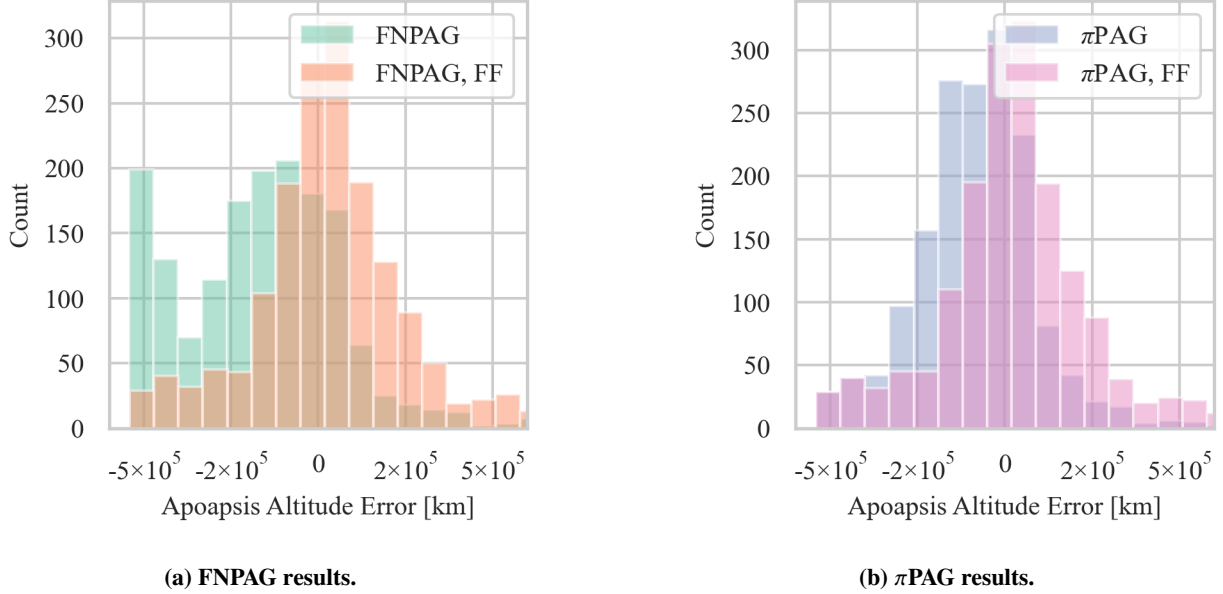


**Fig. 10** Captured apoapsis error histogram comparing  $\pi$ PAG and FNPAG with a first-order fading filter for near-escape cases.

### C. $\pi$ PAG Generalizability to Dispersions Outside Training Data

A common concern with deep learning methods is their limited generalizability to data outside the training set. To determine if the GMVAE is generalizable to data outside its training dispersions, a  $\pi$ PAG Monte Carlo simulation with 2,000 trials was run with a 5% increase in variance given in Table 2. The results of this simulation are shown in Table 10. These results demonstrate that  $\pi$ PAG is capable of recovering the majority of the recoverable cases and reducing apoapsis mean error, despite using a GMVAE trained on lower-uncertainty data. However, the apoapsis radius error standard deviation using  $\pi$ PAG is larger than the standard deviation with FNPAG. This is likely because the GMVAE recovered some highly elliptical cases with high apoapses, resulting in a larger standard deviation.

**Table 10** Near-escape  $\pi$ PAG and FNPAG performance comparison with increased dispersions.

	Capture %	Escape %	Impact %	Recoverable Save %	Mean Capture $r_a$ Err. [km]	Capture $\sigma_{r_a}$ [km]
FNPAG	83.65	16.30	0.05	0.00	1.69e+05	2.77e+06
$\pi$ PAG	84.95	15.00	0.05	68.42	1.66e+05	2.79e+06

## VII. Conclusion

Aerocapture—particularly when targeting outer planets or operating under high uncertainty and limited navigation precision—face significant risks due to trajectory dispersions and environmental variability. Traditional guidance algorithms typically rely on the mean state for decision-making and do not account for the likelihood of failure modes. This can result in mission failure when the true state deviates from onboard predictions, affecting both low-cost missions with large uncertainties and missions with precise navigation solutions. The probabilistic indicator function approach presented here improves upon this by estimating the likelihood of each terminal mode and incorporating that information into the guidance logic. This risk-aware strategy increases the mission success rate by proactively biasing guidance commands away from failure regions, making it a critical advancement for robust autonomous aerocapture in uncertain environments. The method is computationally efficient and straightforward to integrate with existing numeric predictor-corrector algorithms, making it an attractive fault-tolerance addition for guided aerocapture missions.

In this work, a novel probabilistic indicator function predictor-corrector aerocapture guidance algorithm was developed and shown to improve aerocapture success rates under high uncertainty. The algorithm uses a Gaussian Mixture Variational Autoencoder (GMVAE) to predict the probability of capture or escape for a given trajectory, and biases the guidance bank angle commands to increase the chance of capture. The algorithm was shown to be effective in recovering both escape and impact cases, which would otherwise fail with the state-of-the-art Fully Numeric Predictor-Corrector Aerocapture Guidance algorithm. The probabilistic indicator function was compared with a first-order fading memory filter for atmospheric density estimation, and results show that the two approaches can be used in conjunction to improve aerocapture performance. Finally, the generalizability of the probabilistic indicator function was demonstrated by training the GMVAE on lower uncertainty data and successfully applying it to higher uncertainty cases, recovering a significant portion of failures outside the training distribution.

While these results highlight the appeal of incorporating a probabilistic indicator function in guidance, this is just one possible implementation. Future work includes improving the corrective guidance commands by designing a controller to steer the trajectory in latent space. Additionally, this algorithm could be used for other high-uncertainty, multi-modal guidance problems, such as guided skip entry or lunar landing with crater avoidance maneuvers.

## Funding Sources

This work was supported by NASA Space Grant Technology Research Fellowship grant number 80NSSC23K1227. AD's work is supported by the DOE-NNSA under award number DE-NA0003968 and NASA under award number 80NSSC21K1117.

## Acknowledgments

We acknowledge Alexandre Cortiella for providing an early version of the GMVAE codes. Thanks to Jens Rataczak for his help implementing FNPAG and GRAM and guiding discussions on this algorithm, and to Chun-Wei Kong for his assistance with the GMVAE training architecture setup. Artificial intelligence tools were used for LaTeX equation editing, Python coding assistance in figure generation, and language editing to improve clarity and readability.

## References

- [1] Committee on the Planetary Science Decadal Survey, *Vision and Voyages for Planetary Science in the Decade 2013-2022*, National Academies Press, Washington, D.C., 2011.
- [2] Dutta, S., Shellabarger, E., Scoggins, J. B., Gomez-Delrio, A., Lugo, R., Deshmukh, R., Tackett, B., Williams, J., Johnson, B., Matz, D., Geiser, J., Morgan, J., Restrepo, R., and Mages, D., “Uranus Flagship-class Orbiter and Probe Using Aerocapture,” *AIAA SCITECH 2024 Forum*, AIAA, Orlando, FL, 2024. <https://doi.org/10.2514/6.2024-0714>.
- [3] Grace, M. J., and McMahon, J. W., “Two-Stage Polynomial Chaos Expansion: An Extension Of Uncertainty Quantification Techniques For Multi-Modal Distributions in Aerocapture,” *AIAA SCITECH 2022 Forum*, AIAA, San Diego, CA, 2022. <https://doi.org/10.2514/6.2022-1769>.
- [4] Lu, P., Cerimele, C. J., Tigges, M. A., and Matz, D. A., “Optimal Aerocapture Guidance,” *Journal of Guidance, Control, and Dynamics*, Vol. 38, No. 4, 2015, pp. 553–565. <https://doi.org/10.2514/1.G000713>.
- [5] Brunner, C. W., and Lu, P., “Comparison of Fully Numerical Predictor-Corrector and Apollo Skip Entry Guidance Algorithms,” *The Journal of the Astronautical Sciences*, Vol. 59, No. 3, 2012, pp. 517–540. <https://doi.org/10.1007/s40295-014-0005-1>.
- [6] Restrepo, R., Mages, D., Smith, M., Deshmukh, R., Dutta, S., and Benhacine, L., “Mission Design and Navigation Solutions for Uranus Aerocapture,” *AIAA SCITECH 2024 Forum*, American Institute of Aeronautics and Astronautics, Orlando, FL, 2024. <https://doi.org/10.2514/6.2024-0715>.
- [7] Graves, C. A., and Harpold, J. C., “Apollo Experience Report: Mission Planning for Apollo Entry,” NASA, NASA TN D-6725, Houston, TX, Mar. 1972.
- [8] Hage, R. T., “A simulation model for probabilistic analysis of Space Shuttle abort modes,” NASA, NASA TM - 108432, Huntsville, AL, Nov. 1993.
- [9] Rataczak, J. A., Amato, D., and McMahon, J. W., “Density Estimation for Entry Guidance Problems Using Deep Learning,” *Journal of Guidance, Control, and Dynamics*, Vol. 48, No. 5, 2025, pp. 1042–1053. <https://doi.org/10.2514/1.G008498>.
- [10] Sonandres, K. A., Palazzo, T. R., and How, J. P., “Real-Time Density Estimation for Uranus Aerocapture Using Deep Learning,” *AIAA SCITECH 2025 Forum*, AIAA, Orlando, FL, 2025. <https://doi.org/10.2514/6.2025-1709>.

- [11] Albert, S. W., Doostan, A., and Schaub, H., “Onboard Density Modeling for Planetary Entry via Karhunen-Loève Expansion,” *2023 IEEE Aerospace Conference*, Institute of Electrical and Electronics Engineers, Big Sky, MT, 2023. <https://doi.org/10.1109/AERO55745.2023.10115794>.
- [12] Rataczak, J. A., McMahon, J. W., and Boyd, I. D., “Convex Predictor-Corrector Aerocapture Guidance,” *Journal of Guidance, Control, and Dynamics*, 2025. <https://doi.org/10.2514/1.G008685>, published online 1 May 2025.
- [13] Tracy, K., and Manchester, Z., “CPEG: A Convex Predictor-corrector Entry Guidance Algorithm,” *2022 IEEE Aerospace Conference*, Institute of Electrical and Electronics Engineers, Big Sky MT, 2022. <https://doi.org/10.1109/AERO53065.2022.9843641>.
- [14] Zucchelli, E. M., Hanasusanto, G. A., Jones, B. A., and Mooij, E., “Two Stage Optimization for Aerocapture Guidance,” *AIAA SCITECH 2021 Forum*, AIAA, Virtual, 2021. <https://doi.org/10.2514/6.2021-1569>.
- [15] Dilokthanakul, N., Mediano, P. A. M., Garnelo, M., Lee, M. C. H., Salimbeni, H., Arulkumaran, K., and Shanahan, M., “Deep Unsupervised Clustering with Gaussian Mixture Variational Autoencoders,” *5th International Conference on Learning Representations*, International Conference on Learning Representations, Toulon, France, 2017. <https://doi.org/10.48550/arXiv.1611.02648>.
- [16] Miele, A., Zhao, Z. G., and Lee, W. Y., “Optimal Trajectories for the Aeroassisted Flight Experiment. Part 1: Equations of Motion in an Earth-Fixed System,” NASA, NASA-CR-186134, Houston, TX, Jan. 1989.
- [17] Deshmukh, R., Chadalavada, P., Dutta, S., and Lugo, R., “6-DoF Uranus Aerocapture Trajectory Analysis,” *AIAA SCITECH 2025 Forum*, AIAA, Orlando, FL, 2025. <https://doi.org/10.2514/6.2025-1510>.
- [18] Justh, H. L., Cianciolo, A. M. D., Hoffman, J., and Allen Jr., G. A., “Uranus Global Reference Atmospheric Model (Uranus-GRAM) 2024: User Guide,” NASA, NASA/TM - 20240011228, Huntsville, AL, Aug. 2024.
- [19] Matz, D., Johnson, B. J., Geiser, J., Sandoval, S., Deshmukh, R., Lugo, R., Dutta, S., and Chadalavada, P., “Analysis of a Bank Control Guidance for Aerocapture at Uranus,” *AIAA SCITECH 2024 Forum*, AIAA, Orlando, FL, 2024. <https://doi.org/10.2514/6.2024-0717>.
- [20] Brent, R. P., *Algorithms for Minimization Without Derivatives*, Prentice-Hall, Englewood Cliffs, NJ, 1973.
- [21] Lu, P., “Entry Guidance: A Unified Method,” *Journal of Guidance, Control, and Dynamics*, Vol. 37, No. 3, 2014, pp. 713–728. <https://doi.org/10.2514/1.62605>.
- [22] Kingma, D. P., and Welling, M., “An Introduction to Variational Autoencoders,” *Foundations and Trends in Machine Learning*, Vol. 12, No. 4, 2019, pp. 307–392. <https://doi.org/10.1561/22000000056>.
- [23] Cinelli, L., Marins, M. A., da Silva, E. A. B., and Netto, S. L., “Variational Autoencoder,” *Variational Methods for Machine Learning with Applications to Deep Networks*, Springer Cham, Switzerland, 2021, 1<sup>st</sup> ed., pp. 111–149. <https://doi.org/10.1007/978-3-030-70679-1>.

